8th International Conference on Physical and Numerical Simulation of Materials Processing, ICPNS'16
Seattle Marriott Waterfront, Seattle, Washington, USA, October 14-17, 2016

Evaluation of Ductile Fracture Model in Bulk Forming

Miroslav URBANEK[1], Jan DZUGAN[1] and Antonin PRANTL[1]
[1]COMTES FHT, Dobrany, 334 41, Czech Republic

ABSTRACT

The purpose of this study is to evaluate the parameters of material plasticity and fracture models at room temperature and at rates up to 1 mm/min for steels which are ordinarily used for forging, for instance the 38MnVS6 steel. The behaviour of materials during forming was evaluated and described using MARC/MENTAT and DEFORM software tools. Several fracture models were examined from the perspective of the planned research tasks which involve testing at forging temperatures up to 1100 °C. The fracture models considered were those which are implemented as standard tools for example: Cockcroft and Latham, Oyane, and Rice and Tracey. These can be employed for numerical simulations of forging, punching and shearing, the most frequent operations in the manufacture of forged parts.

Standard tensile tests, torsion tests, and compressive tests were carried out. Based on the tensile test data, an FEM analysis of the stress-strain curve was conducted. The ductile fracture models were then calibrated using multiple stress-strain conditions, including triaxial stress states, and various Lode angles.

Tensile and compressive tests were carried out on a Zwick 250 kN testing machine which was provided with the ARAMIS digital image correlation system from the GOM company. For the torsion tests, an MTS Bionix (25 kN and 250 Nm) servohydraulic testing machine was employed.

Keywords: FEM, measurement, triaxiality, normalized Lode angle, Cockcroft-Latham, Oyane

1 INTRODUCTION

The main objective of the present study was to characterize the behaviour of the material of billets from round bars during shearing by means of numerical simulation. An important part of this investigation was measurement of properties of the 38MnVS6 steel using standardized and non-standard test pieces, and their evaluation with the aid of numerical simulation. The first step, however, was a literature search which was carried out in order to map the state of the art, while taking into consideration the capabilities and limits of the testing laboratory at COMTES FHT and the programs intended to be used, MARC/MENTAT and DEFORM. Several geometries of test specimens were found in the literature and their tests were simulated to identify stress states caused in them by imposed loads. For each of these specimens, the resulting stress state was plotted in a graph with axes representing triaxiality and normalized Lode angle. It was also compared with other theoretical and empirical findings from the literature. (Bai, 2008), (Bai & Wierzbicky, 2015)

Using this procedure, various stress states and their effects can be mapped in geometrically simple test specimens and the knowledge acquired can then be employed for predicting the plastic behaviour and failure of material in any bulk forming process.

This study explores the material behaviour at ambient temperature. The next step will focus on the behaviour of the 38MnVS6 steel at elevated temperatures, specifically at forging temperatures when additional process and material begin to play a role as well. Although the 38MnVS6 steel is typically used for making closed-die forgings, and therefore worked at high temperatures, billets for forging are sometimes cut at ambient temperatures.

2 CHARACTERIZATION OF STRESS STATE

When subjected to load, isotropic elastic-plastic materials, whose typical representatives include metals, develop stress states which can in general lead to various responses: elastic deformation, plastic deformation or even failure. Elastic behaviour under tensile load is characterized by Hooke's law. Here, the stress and strain only depend on Poisson's ratio, and Young's modulus. Plastic deformation, is described by a work-hardening curve or plasticity models expressed by equations. Finally, failure is identified using various models, in which development of damage is either coupled with plastic deformation (Gurson, Lemaitre) or separate from deformation (uncoupled models Cockcroft-Latham, Oyane, Tracey-Rice).

In continuum mechanics, stress states can be expressed by various formulas and their associated geometric interpretations: for instance in a cartesian coordinate system forming the principal stress space (σ_1, σ_2, σ_3). A definition of a homogeneous and isotropic material can take the form of three stress invariants written as the following equations.

$$p = -\sigma_m = -\frac{1}{3}(\sigma_1 + \sigma_2 + \sigma_3) = -\frac{1}{3}I_1$$

$$q = \overline{\sigma} = \sqrt{\frac{1}{2}[(\sigma_1 - \sigma_2)^2 + (\sigma_2 - \sigma_3)^2 + (\sigma_3 - \sigma_1)^2]} = \sqrt{3J_2}$$

$$r = \left[\frac{27}{2}(\sigma_1 - \sigma_m)(\sigma_2 - \sigma_m)(\sigma_3 - \sigma_m)\right]^{1/3} = \left(\frac{27}{2}J_3\right)^{1/3}$$

Here, I_1 is the first stress invariant and J_2 and J_3 are second and third deviatoric stress invariants. Authors who study ductile fracture often use special parameters to describe stress states. One of them is the dimensionless hydrostatic pressure η, referred to as triaxiality:

$$\eta = \frac{-p}{q} = \frac{\sigma_m}{\overline{\sigma}}$$

Other parameters include the normalized third stress invariant ξ, the Lode angle ξ,
(within the $0 < \left(\frac{\pi}{3}\right)$ interval) or the normalized Lode angle (within the $-1 < \overline{\theta} < 1$ interval), which are defined by equations given below.

$$\xi = \left(\frac{r}{q}\right)^3 = \cos(3\theta) \qquad \overline{\theta} = 1 - \left(\frac{6\theta}{\pi}\right) = 1 - \frac{2}{\pi}\arccos\xi$$

If a particular stress state were plotted as a point in space, it could be formulated in various ways with corresponding geometric interpretations within appropriate coordinate systems (Figure 1). The first formulation is based on the cartesian coordinate system of the principal stress space (σ_1, σ_2, σ_3), the second relies on the cylindrical coordinate system using the mean stress, hydrostatic pressure and Lode angle (σ_m, $\overline{\sigma}$, θ), and the third one involves the spherical coordinate system with hydrostatic pressure, triaxiality and the Lode angle ($\overline{\sigma}$, η, θ). When used at the same time, all these systems will define an identical stress state but using different mathematical notations and corresponding geometric interpretations.

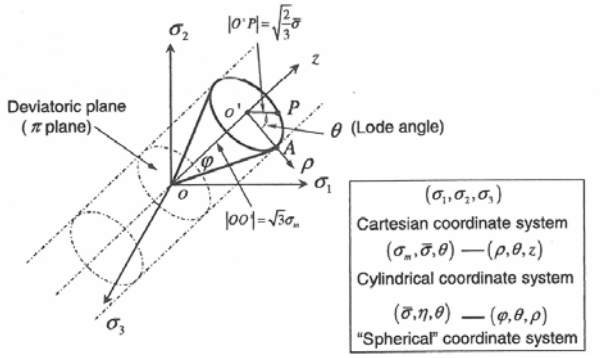

Figure 1 *Three types of coordinate systems in the space of principal stresses (Bai, 2008)*

Some authors use the Lode angle denoted by θ_L and defined it using the Lode parameter μ and principal stress (Xue and Wierzbicki, 2009), (Barsoum and Faleskog 2007a)

$$\mu = \frac{2\sigma_2 - \sigma_1 - \sigma_3}{\sigma_1 - \sigma_3}$$

$$\theta_L = tan^{-1}\left(\frac{1}{\sqrt{3}}\mu\right) = tan^{-1}\left(\frac{1}{\sqrt{3}}\frac{2\sigma_2 - \sigma_1 - \sigma_3}{\sigma_1 - \sigma_3}\right)$$

For comparison with previous relationships, the Lode angle $\theta_L = \theta - \frac{\pi}{6}$ can be expressed for all stress states (Figure 2a), while $\mu = -\overline{\theta}$ holds for the conventional stress states, (Figure 2b).

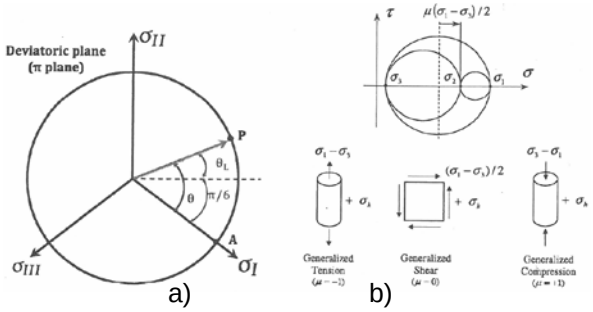

Figure 2 *Other definitions of Lode angle θ_L (a) and normalized Lode angle θ_L (a) and normalized Lode angle μ (b) (Bai, 2008)*

The default set-up of the MSC.MARC/MENTAT 2015 software does not include the definitions of triaxiality and the Lode angle. These variables were therefore user-defined with the aid of the FORTRAN programming language and a user subroutine.

3 DUCTILE FRACTURE INDICATORS

The choice of the appropriate fracture criterion reflected various aspects, including its availability in commercially available computational programs. Ductile fracture criteria are implemented through physical and mathematical models on the basis of experimentally-gathered data. Factors such as the strain path, hydrostatic pressure, and triaxiality have a major impact on materials failure.

Using them, stress states, and even fracture can be described. Generally, a fracture indicator can be viewed as an integral over an interval from zero to the maximum plastic strain which leads to fracture. The variables integrated are damage development criteria based on stress distribution. Fracture models can be divided into two major groups. The first comprises models based on micromechanics, and the other models based on the growth of defects.

Commercially-available programs like DEFORM or MSC. MARC/MENTAT typically use Cockcroft-Latham, Oyane, and Rice-Tracey fracture models which belong to uncoupled models where the growth of defects is not coupled to deformation calculation.

3.1 Models based on growth of defects

The mechanism of nucleation, growth and coalescence of voids is commonly accepted to be the reason for ductile fracture. The criteria in this group use various physics-based concepts, such as void geometry, void growth mechanism and the constitutive material model.

3.1.1 Geometry of defects

One of those mentioned above that belongs to this group is the Rice and Tracey criterion, which uses an analysis of enlargement of spherical voids under a triaxial stress state. It has been successfully employed in studies of cutting.

$$I = \int_0^{e^{pf}} 0.283 exp\left(\frac{\sqrt{3}}{2} \cdot \frac{\sigma_H}{\sigma_{eq}}\right) \; de^p$$

3.1.2 Growth mechanism

Yet another group is represented by the Cockcroft-Latham criterion which assumes that the quantity that is relevant to fracture initiation is the ratio of the largest principal stress and von Mises equivalent stress. For this reason, it is defined by the stress ratio along the strain path.

$$I = \int_0^{e^p} \frac{\sigma_1}{\sigma_{eq}} de^p$$

3.1.3 Material behaviour

The last criterion tested, Oyane, was developed for metal powders and porous materials. It is defined by the ratio of the mean stress and von Mises equivalent stress, and by the constant B. The constant depends on the density of the porous material, and on the density of the pore-free matrix of this material. According to the model, fracture occurs when the sum of triaxiality and the material constant B reaches its threshold value.

$$I = \int_0^{e^{pf}} \left[B + \frac{\sigma_{mean}}{\sigma_{eq}}\right] de^p$$

Since the Cockcroft-Latham and Oyane models are the only fracture models available by default in MARC/MENTAT, they will be the only ones used below.

3.2 Analysis of stress state in test specimens

Drawing on the literature search, suitable geometries of standardized and non-standard test specimens were identified and numerical simulations of their tests were run in order to determine the stress states present in these specimens. The following table gives values of triaxiality and the Lode angle, both theoretical ones, and those computed by simulation. The formulas shown in the table were adopted from (Bai, 2008).

If no theoretical value is given, it means that either no relevant formula was found or none exists. Drawings of individual test specimens are compiled in Figure 3.

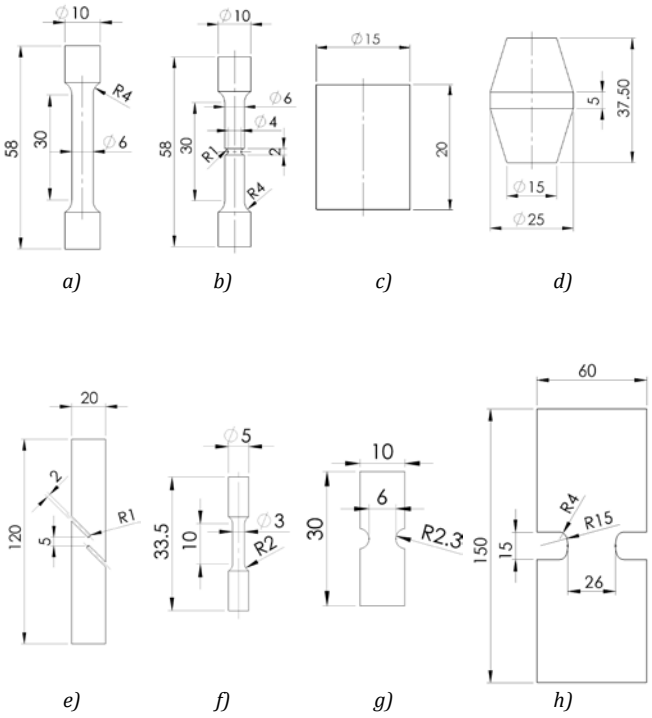

Figure 3 *Geometry of standard and non-standard samples*

Table 1 List of tests carried out

Specimen type		Triaxiality			Norm. Lode angle	
		Formula	Theory	Sim.	Theory	Sim.
Smooth round bars, tension	a)	1/3	0.333	0.33	1	0.99
Notched round bars with radius R1, tension	b)	$\frac{1}{3}+\sqrt{2}\ln(1+\frac{a}{2R})$	1.026	1.01	1	0.61
Smooth round bars, compression	c)	-1/3	-0.333	-0.32	-1	-0.99
Tapered round bars, compression	d)	-	-	0.27	-	-0.13
Shear	e)	0	0	0.02	0	-0.09
Torsion	f)	0	0	0.01	0	0.00
Flat grooved plates, tension	g)	$\frac{\sqrt{3}}{3}+\left[1+2\ln(1+\frac{t}{4R})\right]$	0.688	0.57	0	0.00
Plane strain, tension	h)	$\frac{\sqrt{3}}{3}$	0.577	0.55	0	0.01

Note:
a – radius at the bottom of groove, R – radius of a groove, t – specimen width across the groove

Stress states in the specimens were studied by numerical simulation with the aid of a homogeneous isotropic elastic-plastic material model. Plasticity of the 38MnVS6 steel was characterized by a fitted work-hardening curve based on mechanical tests described below in section 4.4.

In locations of major interest, the element size was approximately 0.1 mm. No element in any of the models exceeded 1 mm. Boundary conditions reflected the set-up in the testing machine and the test sequence. The simulated test speed was approximately 0.0333 mm/s which corresponds to quasi-static testing conditions. Problems involving rotation-symmetric specimens were treated as axially-symmetric problems. Those with flat specimens were approached as either plane stress or plane strain problems.

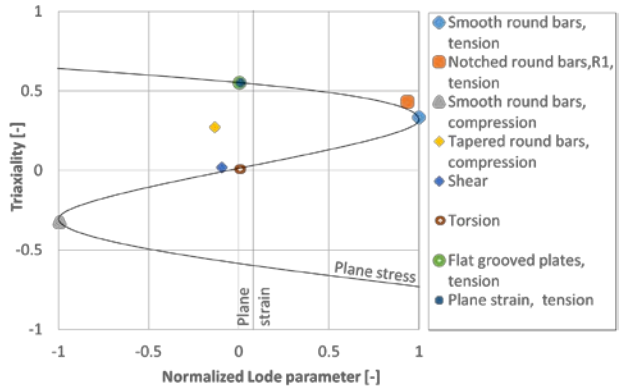

Figure 4 Positions of simulated mechanical tests in (η, ϑ) space

Figure 4 shows a 2D space of triaxiality and normalized Lode angle. The plotted points represent stress states in individual test specimens (those in Figure 3) identified by numerical simulation.

4 STEEL PROPERTIES

4.1 Chemical composition and properties

The 38MnVS6 steel used in this study is a ferritic-pearlitic precipitation-strengthened steel whose strength given by the standard should be in the 800–950 MPa range. Its typical applications include forged machine parts and components for the automotive industry.

Actual chemical composition of the blank was measured using a Bruker Q4 TASMAN optical emission spectrometer. The results reported in Table 2 indicate that it matches the requirements of the standard.

Table 2 Measured chemical composition of 38MnVS6 steel

C	Si	Mn	P	S	Cr	Mo	Ni	Cu	Al	As
0.39	0.60	1.33	0.02	0.05	0.14	0.03	0.08	0.05	0.01	0.01

4.2 Measurement procedure

First, a tensile test was carried out and the test data was input into numerical simulation to generate a true stress-true strain curve (TS-TS curve). Using this TS-TS curve, simulations of compressive test and notched bar tensile test were run. These simulations employed uncoupled models, i.e. those in which a separate plasticity investigation is followed by application of fracture models.

4.3 Mechanical testing

In this study, mechanical properties data were acquired by conducting tensile, compressive and torsion tests. Smooth bar tensile tests were carried out first, followed by tests on notched bars with R1 radius. Then, the flow curve was validated using compressive test, and torsion test was employed to determine the fracture criterion. The choice of these tests was based on the initial analysis of stress states in the various test specimens, the available laboratory facilities, and earlier experience in finding the parameters of material models.

4.4 Tensile test

The smooth and notched bars were tested at ambient temperature and under quasi-static conditions. Using the ZWICK 200 kN machine, the test was carried out at the speed of 2 mm/min. The

smooth round bars had a diameter of 6 mm and a gauge length of 30 mm (Figure 3a). The size of the notched bars was the same, apart from the added notch of 1 mm depth with an R1 radius (Figure 3b). One part of the test record was obtained through a mechanical extensometer with the initial length L_{0ex} of 20 mm for the smooth bars and 10 mm for the notched ones. The extensometer provided the displacement vs. time curve while the machine provided the crosshead displacement and force-time records. Table 3 gives the dimensions and material values for this tensile test.

Table 3 Characteristic dimensions before and after the test

D_0	D_u	L_0	L_u	E	$PS_{0.2}$	UTS	A_5	RA
(mm)	(mm)	(mm)	(mm)	GPa	MPa	MPa	%	%
6.00	3.88	30.0	35.9	212	565	872	19.67	58.18

Note:

D, L – specimen dimensions, E – modulus of elasticity in tension, PS0.2 – proof stress, UTS – ultimate tensile strength, Ag – elongation beyond UTS, A_5 – elongation for 5 mm gauge length, RA – reduction of area, subscripts: 0 – initial value, u – value after test

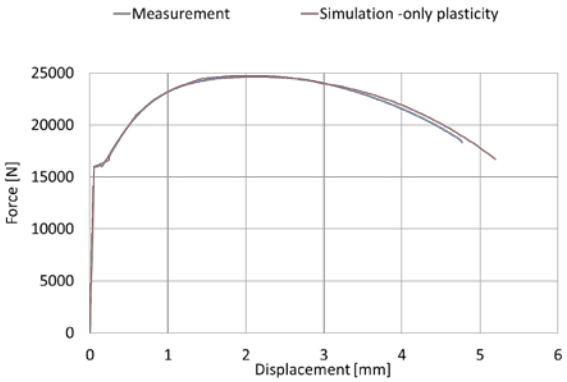

Figure 5 Comparison between tensile test plot and data from the simulated test

After the test, the relationship between force and the deformation measured by the extensometer was evaluated. Using the script described in (Ruzicka, 2016), a stress-strain curve was computed from the measured data. It was then calibrated by FEM simulation to ensure that the simulated material response replicates as faithfully as possible the actually measured response. The calibration conditions were identical to those of the measurement. Thanks to the axially-symmetric geometry of the test, the analysis could be simplified to an axisymmetric 2D problem. The figure below compares the actual and the simulated tensile test plots. The calibration of the TS-TS curve did not take damage in the material into consideration.

The same procedure was applied to the notched bar (shown in Figure 3b) tensile test. Its simulation used the stress-strain curve from the previous test. Table 4 gives the dimensions and material values for this tensile test.

Table 4 Characteristic dimensions before and after the test

D_0	D_u	L_0	L_u	E	$PS_{0.2}$	UTS	A_{50}	RA
(mm)	(mm)	(mm)	(mm)	GPa	MPa	MPa	%	%
4.10	1.00	30.0	31.6	202	839	1191	3.5	94.0

In the figure below, good agreement can be seen between the actual test plot and the simulated tensile test data at the triaxiality of 1/3 and normalized Lode angle of approximately 1.

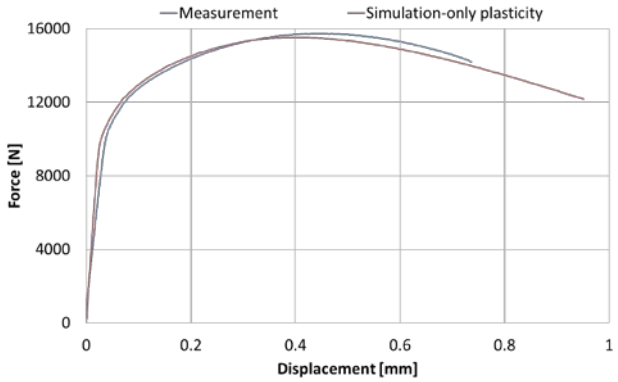

Figure 6 Comparison between tensile test plot and data from the simulated test

4.5 Compression test

The compressive test according to the ISO 13314 standard was performed in an Inova 100 t hydraulic testing machine. Its purpose was to account for the effects of compressive load, and to measure and characterize another stress state.

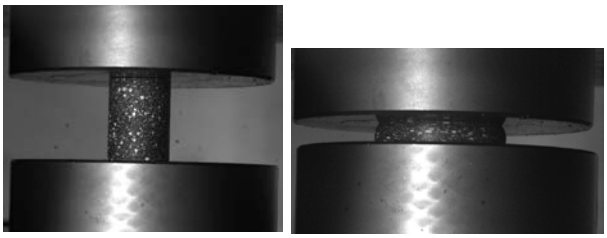

Figure 7 Sample before (left) and after (right) test

The comparison between the test plot and the simulation data confirms a good agreement between the compressive load responses. Nevertheless, the

higher than actual compressive force indicated by the material model must be taken into account when using the calibrated stress-strain curve for the plastic deformation region. The table below reports the dimensions before and after the compression test.

Table 5 Characteristic dimensions before and after the test

D_0	D_u	L_0	L_u
(mm)	(mm)	(mm)	(mm)
15	6.09	20	27.82

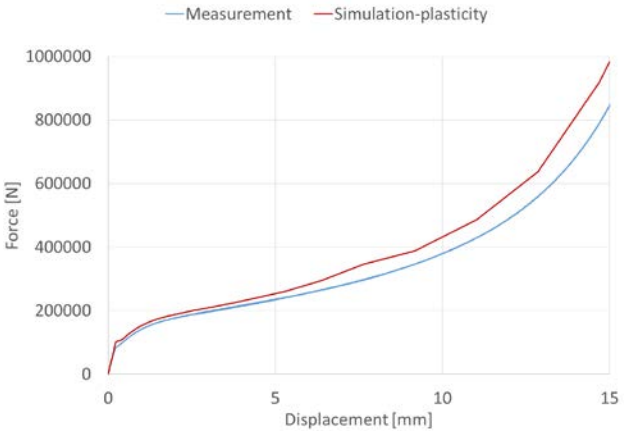

Figure 8 *Comparison between compression test data and data from simulation*

At large strains in a compression test on an outer surface develop cracks. In compression test specimens with an appropriately modified shape, however, fracture can set in much earlier, as reported by several authors (Zheng et al., 2007), and (Pires et al., 2003). One such design was explored in this study – the tapered round bar shown in Figure 3d. Unfortunately, the force needed to achieve the desired strain exceeded the capacity of the available laboratory equipment. This required force magnitude was more than 120 t, and it is the reason which this test specimen is not discussed further.

4.6 Torsion

The last actual conventional mechanical test was the torsion test defined by the ISO 7800 standard where the test specimen is subjected to pure torsion at zero axial force. Because of the small size of the specimen used, the test data could only be obtained from the testing machine record. Neither mechanical torsional extensometer nor digital image correlation could be employed.

The theoretical stress states in torsion and shear are identical and defined by zero values of triaxiality and the Lode angle. The initial numerical analysis revealed that the torsion test on the specimen shown in Figure 3f generates a more homogeneous plastic deformation field than the shear test in the test piece in Figure 3e. Therefore, the actual torsion test used a small-size specimen of 3 mm diameter and 10 mm gauge length. The specimen bent slightly during the test, which distorted the test data. Despite that, the torque data calculated from the piston angle appear to be in relatively good agreement with the simulation, showing that the deflection had no major effects. This simulation relied again on the TS-TS curve calibrated against the tensile test. Due to a different stress state involved, this simulation indicates higher than actual torque values, same as the compressive test simulation. The table below gives the relevant dimensions.

Table 6 Characteristic dimensions before and after test

D_0	D_u	L_0	L_u
(mm)	(mm)	(mm)	(mm)
2.99	3.01	10.02	9.42

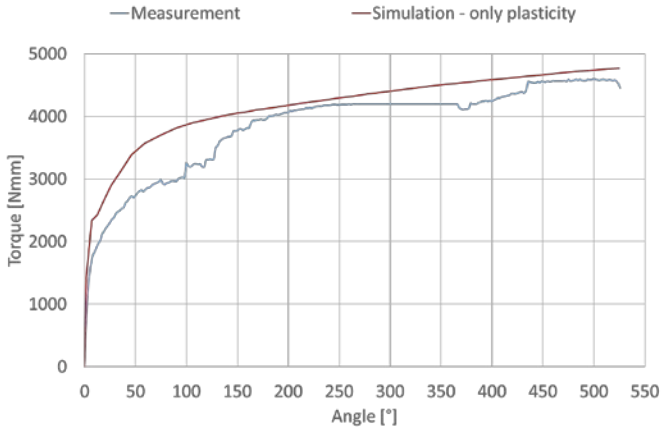

Figure 9 *Comparison of torsion test data*

5 COMPARISON OF DAMAGE MODELS

To identify fracture, two models were used: the Cockcroft-Latham and the Oyane model. It follows from fundamental principles that it is impossible to determine a single universally applicable fracture value. Generally, the fracture strain depends on the stress state and the failure surface is defined by the normalized Lode angle, triaxiality, and fracture strain. Therefore, the materials constants identifying the onset of failure will be determined for particular stress states on the basis of the mechanical tests. The following graphs (Figures 10–12) show the results of numerical analysis. Table 7 lists material constants for both models considered here.

Finding the single constant for the Cockcroft-Latham model was relatively straightforward although different stress states require different values. With the Oyane model, the material constant B was determined iteratively by trial and error for individual stress states. Threshold values for both models were found by the same procedure.

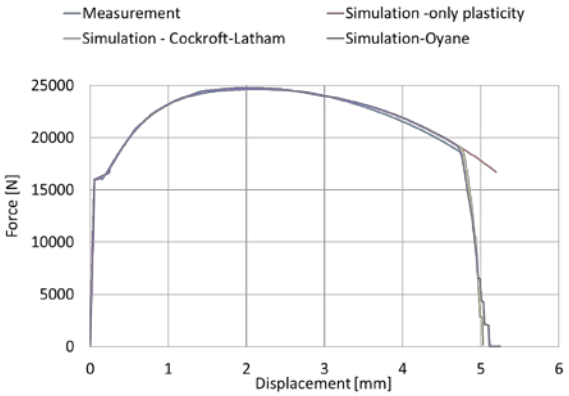

Figure 10 Comparison of tensile test data

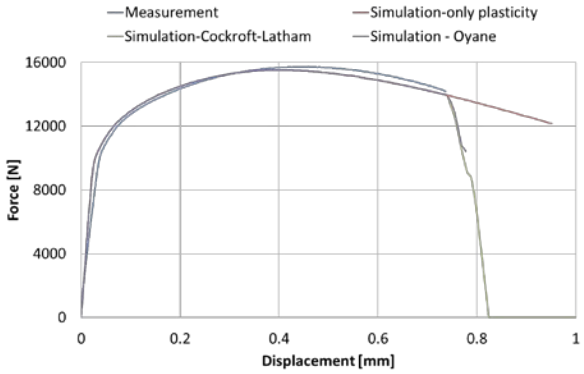

Figure 11 Comparison of tensile test data

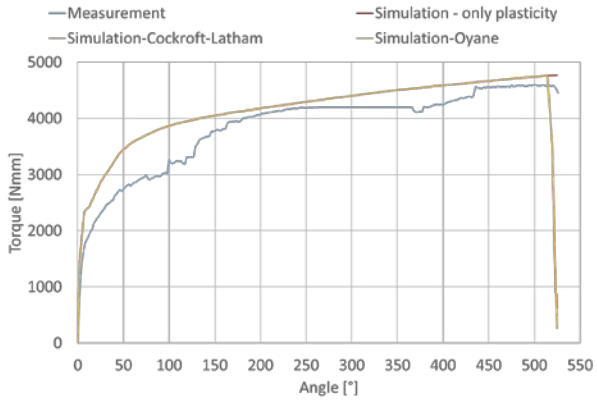

Figure 12 Comparison of torsion test data

Table 7 Parameters of models for various stress states

Model	Cockcroft-Latham	Oyane	
Material constants	e^{pf}	e^{pf}	B
Smooth round bars, tension	0.88	0.75	0.5
Notched round bars with radius R1, tension	0.57	0.48	0.5
Torsion	0.43	0.37	0.5

Individual points on the failure surface for the 38MnVS6 steel for ambient temperature and quasi-static conditions are plotted in 3D space of triaxiality, normalized Lode angle, and fracture strain in Figure 13.

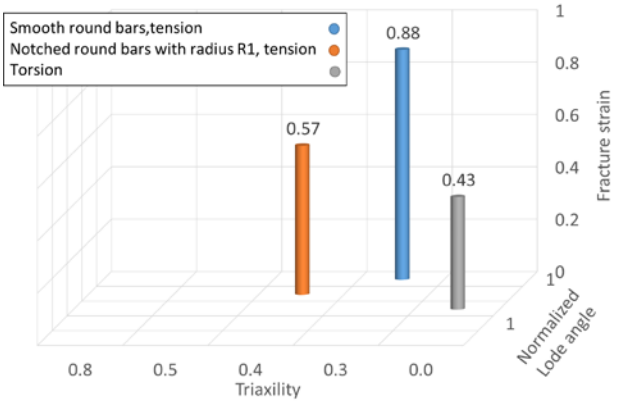

Figure 13 Failure in 3D space defined by triaxiality, normalized Lode angle, and fracture strain

6 VALIDATION BY REAL-WORLD APPLICATION

Several authors have suggested procedures for refining failure surface data but reports on verification of their effectiveness are rare. Authors of this study have therefore dealt with validation of the identified failure surface.

The plasticity model and the fracture values found by basic mechanical tests and numerical analysis were validated by a simple technological test. It involved a special fixture (Figure 14) which was in fact a 1:10 scale model of a real-world tool. The objective was to validate the material model in a real-world process.

Using the CAD model of the fixture (Figure 14) a numerical model of the validation test (Figure 15) was developed, accurately representing the experimental set-up. The test was carried out at

ambient temperature at the punch speed of 90 mm/s. The die was placed on a plate load cell attached to the frame of an MTS 810 testing machine. The punch was connected to a moving piston and the test specimen of 10 mm diameter was placed into the fixture. The die clearance was 0.05 mm in accordance with the applicable standard. In the simulation model, the material was considered to be homogeneous, isotropic and elastoplastic. Its plasticity was characterized by the calibrated TS-TS curve. With regard to the expected dominance of the shear failure mechanism, the fracture model used for the first FEM simulation run was the Cockcroft-Latham model with a damage threshold of 0.43.

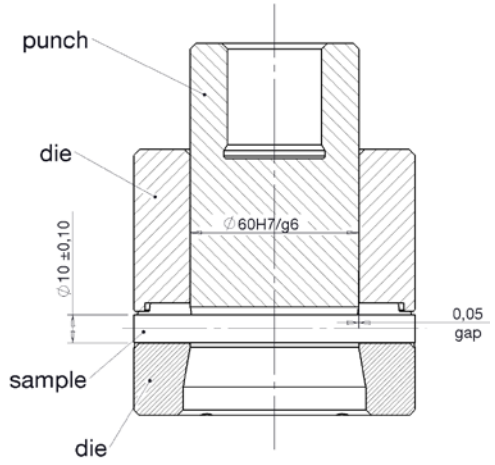

Figure 14 *Set up of technological test a) drawing b) CAD model*

The parts of the fixture were considered rigid bodies for the calculation. The model of the specimen comprised only one quarter of the actual piece (because its two symmetry planes) and was divided into three parts: the inside, the outside, and the central part. The shear plane was in the central part, which had a much finer mesh than the other parts of the model. The size of elements in the vicinity of the shear plane was 0.05–0.2 mm, as opposed to the 1 mm size used elsewhere.

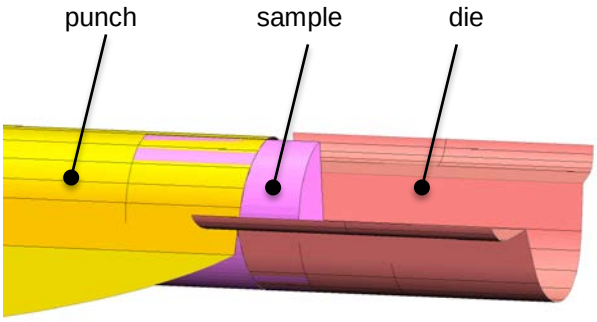

Figure 15 *¼ FEM model*

According to the plot in Figure 16, the stress state induced by the validation test is close to those existing in torsion and compression tests. For this reason, the fracture model parameters chosen from Table 7 were those for the torsion test (Cockcroft-Latham e^{pf}=0.43 and Oyanee^{pf}=0.37, B=0.5).

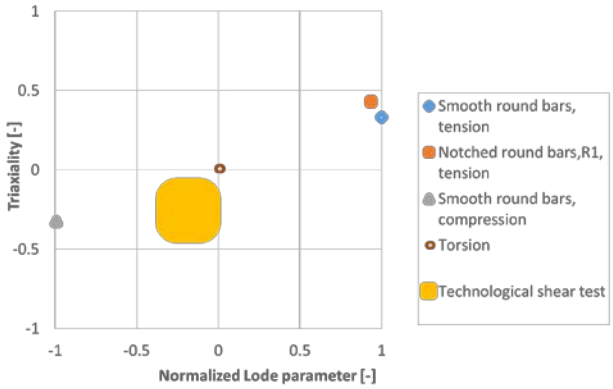

Figure 16 *Position of the technological shear test in (η, ϑ) space*

Figure 17 with superposed results of calculation and the actual test shows that the chosen fracture strain value of 0.43 gives an adequate prediction of material behaviour. The visible minor discrepancy is caused by the initial assumption that pure shear state will exist in the test specimen being sheared. In reality, the actual combined loads cause deviation from that state. If the fracture criterion were to be determined more accurately, the actual process would have to be simulated to identify the actual stress state involved – or a larger number of specimens tested in various stress states.

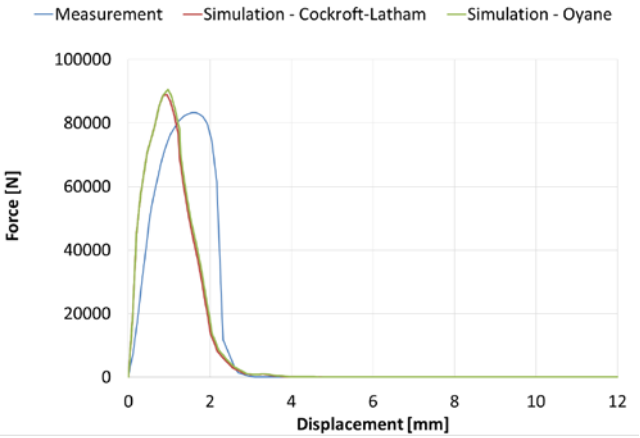

Fig. 17 Comparison of results of validation technological test

7 CONCLUSION AND DISCUSSION

Fracture prediction plays an important role in the design of structural parts or, as in this case, in describing a shearing process. This study presents a procedure for identifying points on the failure surface and using the failure surface in practice. Numerical simulations were performed with the use of uncoupled models. Plasticity was characterized by a TS-TS curve which was derived from a tensile test data. The fracture models used here were based on plastic deformation and triaxiality. Their material constants were identified by measurements of various stress states. Thanks to carefully chosen test piece geometries, fracture initialization occurred in accordance with predictions from individual models. The measured and simulated data were in good agreement in all experiments.

The validation technological test showed agreement between measurement and numerical simulation. In addition, it proved the usability of the chosen method of identifying failure surface points in similar applications.

As mentioned in the introduction the 38MnVS6 steel employed here is frequently used for closed-die forgings. For this reason, the next step will involve measuring and evaluating an identical set of test at temperatures between 950 and 1150 °C. The objective will be to map the effects of temperature on the failure surface and compare results obtained at different temperatures.

REFERENCES

S. Alexandrov, Y.Mustafa, and M. Y. Yahya, An Efficient Approach for Identifying Constitutive Parameters of the Modified Oyane Ductile Fracture Criterion at High Temperature, Mathematical Problems in Engineering, Volume 2013 (2013), Article ID 514945, 4 pages, http://dx.doi.org/10.1155/2013/514945

Y. Bai, T.Wierzbicky, A comparative study of three groups of ductile fracture loci in 3D space, Enginnering Fracture Mechanics 135, ISBN 0013-7944, 2015 p. 147-167

Y.Bai, Effect of Loading history on necking and Fracture, doctoral thesis, 2008

I. Barsoum, J. Faleskog, *Rupture mechanisms in combined tension and shear—Micromechanics*. International Journal of Solids and Structures, Vol. 44, Issue 17, 2007, s. 5481–5498, ISSN 0020-7683.

D. Depriester, E. Massoni, On the damage criteria and their critical values for flowforming of ELI grade Ti64, Metal Forming (http://www.dorian-depriester.fr/Public/MetalForming-Depriester_Massoni_14.pdf)

J. Dzugan, et al., *Identification of ductile damage parameters for pressure vessel steel*. Nucl. Eng. Des. (2015), http://dx.doi.org/10.1016/j.nucengdes.2015.12.014

S. M. Graham, T. Zhang, X. Gao, M. Hayden, *Development of a combined tension–torsion experiment for calibration of ductile fracture models under conditions of low triaxiality*, International Journal of Mechanical Sciences, Vol. 54, Issue 1, 2012, s. 172–181, ISSN 0020-7403

P. Kubik, F. Sebek, J. Petruska, J. Hulka, J. Ruzicka, M. Spaniel, J. Dzugan, A. Prantl, *Calibration of Selected Ductile Fracture Criteria Using Two Types of Specimens*, Key Engineering Materials, ISSN: 1662-9795, 2013, Vol. 592-593, pp.258-261.

Y. Li, E. Onodera and A. Chiba – friction coefficient in hot compression of cylindrical sample

F.M.A. Pires, J.M.A. Cesar de Sa, L. Costa Sousa, R.M. Natal Jorge, *Numerical modelling of ductile plastic damage in bulk metal forming,* International Journal of Mechanical Science 45, 2003, ISSN: 0020-7403, p. 273-294

J. Růžička, Metodika kalibrace nesvázaných modelů a stochastický přístup v problematice tvárného porušování , doctor thesis, 2016

M. Španiel, A. Prantl, J. Džugan, J. Růžička, M. Moravec, J. Kuželka: *Calibration of fracture locus in scope of uncoupled elastic–plastic-ductile fracture material models*, Advances in Engineering Software, Volume 72, June 2014, p. 95-108

M. Urbánek, F. Tikal, Effective Preparation of Non-linear Material Models by Using Programmed Optimazation Script for Nurimerical Simulation of Sheet Metal Processing. In: Materiali in technologije 2, 2/2015. Ljubljana, 2015. p. 5/291-295. ISSN 1580-294.

M. Urbánek, P. Hronek, B. Mašek, P. Nesvadba, The Use of Explosive Energy for Joining Advanced High Strength Low Alloy Steels. In: Journal of Materials Engineering and Performance, Volume 22. Wisconsin, 2012. p. 5/748-752. ISSN 1059-9495

C. Zheng, J.M.A. Cesar de Sa, F.M.A. Pires, *A comparison of models for fracture prediction in forging process*, Computer methods in material science, Vol.7, 2007, No.4, ISSN: 1641-8581, p. 389-396